Construction and Building Materials 392 (2023) 131727

Contents lists available at ScienceDirect

Construction and Building Materials

journal homepage: www.elsevier.com/locate/conbuildmat

Size-scale effects and modelling issues of fibre-reinforced concrete beams

Raffaele Cucuzza [a], Angelo Aloisio [b,*], Federico Accornero [a,c], Antonella Marinelli [a], Elisa Bassoli [d], Giuseppe Carlo Marano [a]

[a] Politecnico di Torino, DISEG, Dipartimento di Ingegneria Strutturale, Edile e Geotecnica, Corso Duca Degli Abruzzi, 24, Turin, 10128, Italy
[b] Università degli Studi dell'Aquila, Civil Environmental and Architectural Engineering Department, via Giovanni Gronchi 18, L'Aquila, 67100, Italy
[c] Shantou University, College of Engineering, University Road, 243, Shantou, 515063, China
[d] Università degli Studi di Modena e Reggio Emilia, DIEF, Engineering Department "Enzo Ferrari", via Università, 4, Modena, 41121, Italy

ARTICLE INFO

Keywords:
Fibre-reinforced concrete
Size-scale effects
Brittleness
Fracture mechanics
Numerical analysis
OpenSees

ABSTRACT

This paper compares numerical and analytical predictions for the shear capacity of fibre-reinforced concrete beams based on experimental literature tests. The authors compared the outcomes of a FE model using the DamageTC3d constitutive model, a literature formulation, and the current proposal of the Eurocode 2 draft for fibre-reinforced structures. The paper evaluates the sensitivity of the beam response to the fracture energy G_f, modified after the Model Code 2010 formulation. The investigation reveals a dependence of the estimated fracture energy on the beam size. Furthermore, the comparison between the numerical estimates and the analytical predictions using the MC2010 and the current EC2 draft proves that the error is substantially independent of the model selection but is strongly affected by the specific case study. This fact confirms the absence of weaknesses in the numerical modelling and highlights the aleatoric uncertainties of the experimental data.

1. Introduction

The development of modern building engineering and infrastructure development demands high material performance, which means high strength, toughness, and energy absorption ability. High-Performance Concrete (HPC) and Ultra High-Performance Concrete (UHPC) represent examples of new materials that are capable of reaching an ultimate compressive strength between 120 and 240 [2,3]. The improvement of mechanical properties, such as strength, workability and durability, is allowed by the integration of supplementary cementitious materials such as silica fume (SF), ground granulated blast-furnace slag (GGBS), fly ash (FA) [4]. Furthermore, reaching high strength also has negative impacts due to increased concrete brittleness, which adding fibres can mitigate. The mixture which combines HPC and fibres is called High-Performance Fibre Reinforced Concrete (HPFRC) or Ultra-High-Performance Fibre Reinforced Concrete (UHPFRC) depending on the ultimate compressive strength achieved [5]. The distinction between the various types of fibre-reinforced concrete (FRC) could be based on the compressive strength range, as shown in Fig. 1. The FRC has less promising performance than the HPFRC and UHPFRC as they are implied for different fields of applications. Indeed, the FRC is cheaper than the others, and it pushes the researcher to keep on investigating its behaviour since it is widely used in the community of practitioners. In 2010, Model Code 2010 [6] acknowledged fibre-reinforced concrete (FRC) as "a composite material made by a cement matrix and discrete fibres. The matrix could be mortar or concrete while the fibres can be made of steel, polymers, carbon, glass or natural fibres". Recently, new international standards, see the new draft of Eurocode 2 [7] and the new Model Code 2020 [6], consider FRC and High-Performance-Fibre-Reinforced-Concrete (HPFRC) as new building materials. Furthermore, several national standards such as the French code NF P18 [8], the Swiss code SIA 2052 [9], the American code ASTM C1856 [10] and the Japanese code [11] provide directions on the application of UHPFRC. A brittle behaviour characterizes plain concrete in tension due to the low tensile strength, and the reduced strain capacity [7]. Since the first research by Romualdi and Batson [12], the addition of randomly distributed fibres to plane concrete has been shown to provide higher ductility and strength [13]. The fibres transfer stresses between the concrete matrix and tensile strains during the crack propagation, thus improving the post-cracking response [14–17]. The main parameters affecting the design and performance of FRC are the fibre volume content (V_f), the ratio between the length and the diameter of fibres (l/d) and the fibre weight ratio (FWR), defined as the weight of the fibres in 1 m^3. In particular, the l/d ratio affects the number of fibres which cross the cracks under load, keeping constant V_f.

Due to the importance of the fibre dimensions, the industry makes available different types and sizes of this reinforcement, ranging from

* Corresponding author.
E-mail address: angelo.aloisio1@univaq.it (A. Aloisio).

https://doi.org/10.1016/j.conbuildmat.2023.131727
Received 4 December 2022; Received in revised form 12 April 2023; Accepted 7 May 2023
Available online 27 May 2023

Lists of symbol and notation

Latin upper case letters

D_{lower}	Smallest value of the upper sieve size D in an aggregate for the coarsest fraction of aggregates in the concrete permitted by the specification of concrete
E	Elastic Modulus of concrete;
$F^{in}(t)$	Vector of internal nodal forces;
G_f	Fracture Energy;
G_t	Tensile Fracture Energy STKO input;
G_c	Crushing Energy according to MC2010 formulation;
$G_{f,opt}$	Optimum value of G_f;
P_{cr}	First cracking load;
P_u	Ultimate load at the peak;
$P_{u,exp}$	Experimental Ultimate Capacity;
$P_{u,num}$	Numerical Ultimate Capacity;
$R(t)$	Vector of external nodal forces;
S_1	Linear branch slope;
S_2	Nonlinear branch slope;
V_u	Ultimate shear resistance;
W	Elastic Inertia modulus;

Latin lower case letters

b_w	Minimum width of the cross section;
d	Effective depth of a cross section;
d^+	Positive damage index;
d^-	Negative damage index;
d_{dg}	Size parameter describing the crack and the failure zone roughness taking account of concrete type and its aggregate properties;
f_{c0}	Elastic concrete threshold according to STKO damageTC3d
f_c	Compressive strength of concrete;
f_{ck}	Characteristic concrete cylinder compressive strength;
f_{cm}	Mean concrete cylinder compressive strength;
f_{cp}	Concrete peak strength;
f_{cr}	Residual strength equal to 20% fo f_{cm} [1];
f_{ctm}	Mean flexural tensile concrete strength;
f_{ctk}	Characteristic concrete tensile strength;
f_{Ftu}	Residual strength significant for ULS;
$f_{R,3}$	Residual tensile strength at w equal to 2.5 mm;
f_t	Uniaxial tensile strength equal to 2/3 f_{ctm};
f_{Ftuk}	Characteristic values of the ultimate residual tensile strength for FRC, considering the rigid-plastic approach;
f_{Ftud}	Design values of the ultimate residual tensile strength for FRC, considering the rigid-plastic approach;
$f(x)$	Objective Function (OF);
f_y	Yielding steel strength;
$g_q(x)$	Constrain Function (CF) for inequality constraints;
$h_r(x)$	Constrain Function (CF) for equality constraints;
k	Equal to 1 + $(\frac{200}{d})^0.5$, for considering size effect
l	Span length;
l_{cs}	Critical length;
t	Time loading step;
w_{lim}	Crack opening width corresponding to ULS;
x	Design Vector (DV) strength;
z	Inner lever arm of internal forces;

Greek letters

γ_c	Partial factor for concrete;
γ_F	Partial factor for actions, also accounting for model uncertainties and dimensional variations;
γ_V	Partial factor for shear and punching resistance without shear reinforcement;
δ	Displacement at peak load;
η	Ratio of strains used to define stress strain model;
ν	Poisson's ratio;
ρ_l	Reinforcement ratio for bonded longitudinal reinforcement in the tensile zone due to bending referred to the nominal concrete area $d \cdot bw$;
σ^+	Positive stress tensor;
σ^-	Negative stress tensor;
σ_{cp}	The average axial stress on the cross section induced by prestressing;
$\tau_{Rd,cmin}$	Minimum shear stress resistance allowing to avoid a detailed verification for shear (average shear stress over a cross section);
$\tau_{Rd,cf}$	Shear stress resistance of planar members with shear reinforcement subjected to concentrated forces;
ϕ	Diameter longitudinal bar;

Units

Stress and material strengths	For unit dependent, MPa shall be used
E-modulus	For unit dependent, MPa shall be used
Geometric data	For unit dependent, mm shall be used.

6 to a maximum length of 80 mm and from 0.1 to a maximum cross-section area of 1.5 mm^2 [18]. Although this material has been widely adopted in general constructions for some time, in the past, FRC was reluctant for specific construction typologies due to the industry's lack of trust in its functionality [19]. However, steel fibres are among the most used solutions for obtaining FRC [20]. Engineers and builders consider this material a suitable solution, especially for statically indeterminate structures where stress redistribution occurs [21,22]. The benefits of using FRC affect the compression [23,24] and tension behaviour [25,26]. Already in 1996, a collection of the most promising fibre mix-designed was listed in the comprehensive state-of-art by Zollo in [27]. The author, according to the terminology adopted by the American Concrete Institute (ACI) Committee [28], distinguished four different categories of FRC based on fibre material type: SFRC for steel fibre; GFRC for glass fibre; SNFRC for synthetic fibre, including carbon fibres and NFRC for natural fibre. More recently, in [29], the authors tested two types of acro-synthetic fibres obtained by processing natural PP homo polymer

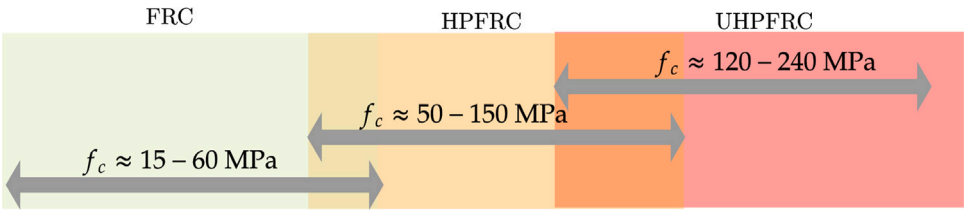

Fig. 1. Compressive strength range for distinction between FRCs.

(density of 910 kg/m^3). Unfortunately, despite the remarkable results, they did not succeed in finding better flexural, shear and ductility behaviour than steel fibres. In [30], Pour et al. presented the results of the first experimental research on the axial compressive behaviour of ultra-high-strength steel (UHSS) fibre-reinforced concrete-filled FRP tubes (UHSSFR-CFFT). Twenty-four circular UHSSFRCFFT specimens were prepared and tested under axial compression to study the influence of unconfined concrete strength and fibre type. CFFTs were manufactured with glass, carbon and basalt-reinforced polymer (GFRP, CFRP and BFRP) tubes with concrete compressive strength ranging from 35 to 105 MPa. Sun et al. [31] investigated the flexural behaviour of six concrete beams with various reinforcements, including ordinary steel bars, steel-fibre reinforced polymer composite bars, and pure fibre-reinforced polymer bars. (either carbon fibre-reinforced polymer bars or basalt fibre-reinforced polymer bars), and hybrid bars (steel bars and basalt fibre-reinforced polymer bars). In all the cases investigated by the authors, the results showed that steel-fibres reinforced polymer increases the ultimate load capacity by approximately 31% and the durability in comparison with traditional RC. Olivito e Zuccarello [32] found that the most crucial contribution of steel fibres is the altering the failure mode from fragile to ductile due to the bridging effects of the fibres, which preserve the specimen integrity for higher strain values. Additionally, short fibres increased the compression strength more than the longer ones [33]. Besides, the main drawback of FRC is the workability reduction of concrete, which can be mitigated using short fibres [34]. Nonetheless, Koksal et al. [20] found that a significant amount of fibres must be added to observe a meaningful improvement in the concrete compression strength. This aspect is confirmed by [4], who showed that a low content of fibres does not affect the peak of the concrete strength. Conversely, the fibre embodiment does not significantly improve tensile strength [35], since their effect manifests after the first crack formation [36]. Nonetheless, the fibres modify the tensile failure mode, depending on the fibre slip, elongations and strengthening associated with three bond mechanisms: adhesion, friction, and mechanical anchorage [37]. Walraven found that the fibres significantly stabilize the crack formations [38]. Accordingly, the Model Code 2010 (MC2010) suggests adopting two different stress–crack relationships: rigid-plastic and linear softening or hardening [6]. The fibre embodiment also improves flexural strength related to the improved compression and tensile response. For instance, Abbass et al. [38] found that the flexural strength of concrete with steel fibres between 0.5% to 1.5% volume ratio increased from 100% to 150%. Additionally, Lee et al. [39] observed that the stress level decreases significantly after concrete cracking based on the fibre volume and concrete compression strength. Consequently, the fibres also improve beam stiffness during the post-cracking phase [40]. Adding steel fibres to the concrete matrix increases the material energy adsorption [41]improving the cracking behaviour and the loading capacity [42–44]. Among the possible physical entities, the fracture energy is the most used in constitutive models for characterizing concrete post-cracking behaviour [41,45]. The reliability and accuracy of non-linear behaviour depend on G_f, which represents the energy necessary to create a unit area of a crack. Besides, if the fibres increase the energy adsorption, the G_f is the parameter that makes the difference between PC and FRC [46,47]. Furthermore, the G_f represents the material toughness, and it is estimated with a three-point bending test on notched standard samples, following the EN recommendations.

As a final remark, the fibres also improve the shear resistance. Additionally, their embodiment leads to a ductile shear failure mode. The fibres guarantee a more uniform bridging effect over the cracks and, in principle, could be considered an alternative reinforcement to the stirrups. Meda et al. [48], and Dang et al. [49] found that the fibres represent a valid and trustworthy alternative to traditional shear reinforcements. Furthermore, J. A. Torres et al. [50] observed that a 1.2% fibre content changes the failure mode from shear to shear-flexural cracks. A higher fibre content leads to more inclined cracks with a 24% shear capacity increment if the fibre volume spans between 0.0% and 1.2%. Additionally, Minelli et al. [51] observed that the fibres can mitigate the size effect in deep beams.

However, despite the numerous experimental tests on UHPC beams, a few studies deal with the FE modelling of FRC beams using constitutive damage models. Thai et al. in [52] presented a calibration of the well-known Karagozian & Case Concrete (K&C) model developed by Malvar et al. [53], which can be applied to describe the complex static and dynamic behaviour of the fibre reinforced concrete (FRC) structures subjected to static and high-rate loading conditions. Gravina et al. in [54,55] investigated the influences of matrix strength, fibre shape and fibre volume fraction on the rate sensitivity of SFRC by developing a 3D finite element model to demonstrate the effectiveness and feasibility of the proposed dynamic increase factor (DIF) formula.

However, to the authors' knowledge, there needs to be research attempting to optimize the constitutive parameters of damage models for FRC to achieve a good agreement with experimental data. Additionally, no research papers attempt to address the modelling of size-effect phenomena in FRC. Therefore, this paper presents and discusses the FE modelling of the concrete beams tested by [51] using the damage TC3d constitutive model based on a nonlinear fracture mechanics approach. The authors selected the specimens tested by Minelli et al. which showed the mitigation of the size effect in the shear capacity of FRC beams. The research question of this paper is: If possible to grasp the size effect in the shear response of FRC with the finite element model using a damageTCrd concrete model and a classical elastic–plastic relationship for steel? The goal is to optimize the fracture energy value using the ultimate capacity of all the tests on FRC beams as an objective function. Starting from the fracture energy value suggested by the MC2010, the authors will provide a final expression for the fracture energy valid for the considered test set. Despite the fact that fracture energy is, by definition, a material property, the authors found that the variation pf the fracture energy compensates for the lack/reduced size effect in FRC. Additionally, the paper compares the capacity predictions from FE models against the estimate according to the new draft of Eurocode 02. The paper has the following organization, after a brief introduction to the test by Minelli [51], the authors will introduce the problem and present the FE model. Then, the results and the comparison with analytical, numerical and experimental values are reported and discussed.

2. Description of the case study

The authors used the beams tested by Minelli et al. [51] as a reference case study. They investigated the effect of steel fibres on the

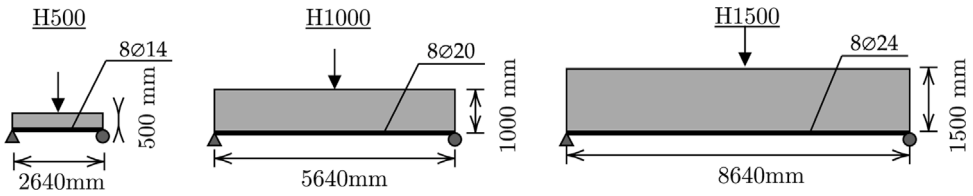

Fig. 2. Geometric characteristics of Minelli's specimens.

Table 1
Characteristics of Minelli's specimens.

Parameters	Dimension	H500	H1000	H1500
Height	[mm]	500	1000	1500
Effective depth	[mm]	440	940	1440
Total length	[mm]	3000	5900	9000
Span	[mm]	2640	5640	8640
Shear span a	[mm]	1320	2820	4320
Width	[mm]	250	250	250
Bottom to rebar centroid distance	[mm]	60	60	60
Reinforcement longitudinal bars		8⌀14	8⌀20	8⌀24
Reinforcement area	[mm^2]	1232	2513	3619
Reinforcement ratio	%	1.12	1.07	1.01

shear response of concrete members. Nine beams were tested under three points bending test with a shear-depth ratio of 3. The beams were obtained with three amounts of fibres: 0, 50 and 75 kg/m^3. For each type of concrete, the authors cast three beams with different heights: 500 (H500), 1000 (H1000), 1500 (H1500) mm and 250 mm thickness. The distance between the bottom beam and the rebar's centroid equals 60 mm. Consequently, the effective depths are 440, 940 and 1440 mm. Fig. 3 shows the geometric characteristics of the specimens. The longitudinal reinforcement layout is realized by two levels of four rebars, ⌀14 for H500, ⌀20 for H1000 and ⌀24 for H1500 and the reinforcement ratio was fixed as approximately 1% for all test specimens. The variability of the bond surface associated with bars with different diameters has not been considered. The bars are anchored at the end by two steel plates. The three concrete types are labelled PC, FRC50 and FRC75 for no fibres and 50 kg/m^3 and 75 kg/m^3 fibre content, respectively. They used a normal-strength concrete with a nominal characteristic strength (f_{ck}) equal to 30 MPa. Table 1 lists the mechanical characteristics of the concrete. The yielding and tensile ultimate strength of longitudinal rebars is 506 and 599 MPa for ⌀14 bars, 555 and 651 MPa for ⌀20 bars, and 518 and 612 MPa for ⌀ 24 (see Fig. 2).

It must be remarked that not only the height and length of the beams change but also the reinforcement. Therefore, this choice is not ideal for estimating the size effect related to the fibre concrete, as highlighted in the discussion section. Additionally, the width is kept constant to reduce the number of variable parameters.

3. FE model

This section provides a synthetic description of the numerical model used in the analysis.

3.1. The DamageTC3d constitutive model

The constitutive model adopted within the analysis is the DamageTC3d model proposed by [56] and implemented in STKO Opensees©. This model defines the tensile and the compressive behaviour, the damage evolution and the failure criteria. The constitutive model for the concrete is a damage model with two parameters d^+/d^-, following [57]:

$$\sigma = (1-d^+)\bar{\sigma}^+ + (1-d^-)\bar{\sigma}^- \tag{1}$$

where $\bar{\sigma}^+$ and $\bar{\sigma}^-$ are the positive and negative stress tensors. d^+ and d^- indicate the damage indices of concrete in tension and compression, respectively [57–59]. They influence the calculation of the positive and negative components of the stress tensor. They are scalars in the range 0–1, indicating the deterioration status of the concrete: if the parameter is 0, the material is intact, while if one, the material is wholly damaged [57]. The damage indices $\bar{\sigma}^+$ and $\bar{\sigma}^-$ are obtained from the concrete behaviour in tension and compression, which can be evaluated through the stress–strain curves of the material. The tensile behaviour of the concrete is characterized by a linear elastic phase up to the tensile strength. After the attainment of the tensile strength, the material shows a softening-like trend, i.e. a decrease in resistance as the deformation of the material increases up to complete failure. [57] provides the full details of the model.

The DamageTC3d model implemented different tensile and compressive behaviour for concrete. The compressive uniaxial law is reported in 3. On the other hand, the tensile behaviour is linear until the ultimate admissible tensile stress; after that, it is described by a nonlinear branch. The area below the curve is the fracture energy G_f divided by the critical length l_{cs}. After a convergence analysis, the mesh size is assumed to equal the critical length. The input parameters of the DamageTC3d constitutive model are G_f and G_c, evaluated by the authors according to the MC2010 formulation, respectively, for normal concrete and FRC. To describe the compression behaviour, the MC2010 provided the same formulation for evaluating the crushing energy for both normal concrete [6]:

$$G_c = 250 \cdot G_f. \tag{2}$$

The authors adopted for G_c the approximate expression in Eq. (2), validated for normal concrete. This approximation is due to the lack of acknowledged formulation for G_c in the scientific literature and the low sensitivity of the shear capacity of fibre-reinforced concrete beams on G_c compared to G_f.

Two different formulations are adopted for normal concrete and FRC tensile behaviour, respectively. In normal concrete, the tensile fracture energy is:

$$G_f = 73 \cdot f_{cm}^{0.18}. \tag{3}$$

For fibre-reinforced concrete, The MC2010 suggests two possible $\sigma - w$ diagrams, where σ and w indicate the tensile stress and crack width, respectively: linear softening/hardening and constant. In this paper, the authors used the $\sigma - w$ relationship with no hardening (see Fig. 4). The stress tension f_{Ftu} is evaluated as 1/3 of the residual tensile strength at a crack width equal to 2.5 mm ($f_{R,3}$), assumed equal to XXXMPA, following [22]. The maximum crack width w_{lim} is set equal to 2.5 mm as MC2010 recommends [6]. The steel stress–strain relationship has been modelled with the material model *Steel01*, which assumes an elastoplastic response. The input parameters are the yielding stress f_y and the elastic modulus E. The values adopted result be the same as those reported in the reference case study. The steel plates at the beam support (see Fig. 5) are modelled as an elastic isotropic material where Young's modulus E = 210 GPa and Poisson's ratio ν = 0.3. Table 2 lists the input parameters used for the concrete and steel constitutive behaviour.

The problem is non-linear type due to the areas of discontinuity and non-linearity of the material. In the FE problem, the solution is obtained

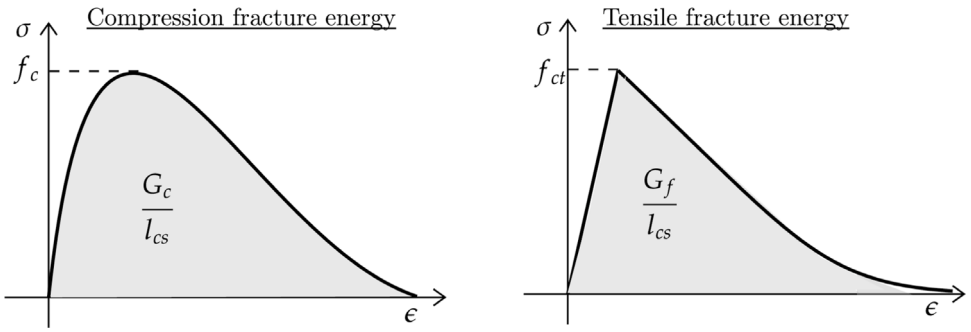

Fig. 3. Stress–strain relationship in tension (a) and compression (b) available in STKO DamageTC3d, where l_{cs} is the critical length.

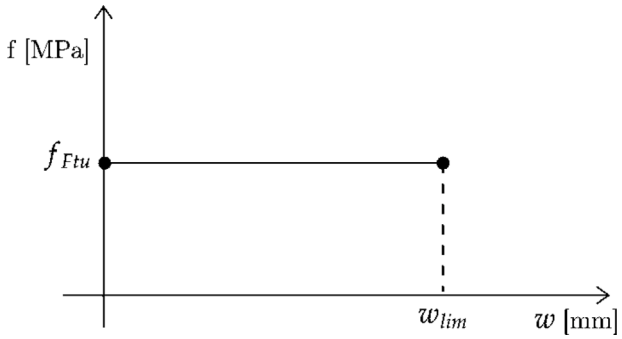

Fig. 4. Stress–crack opening displacement curve chosen for FRC50 and FRC75.

Table 2
Input parameters for the concrete and steel constitutive behaviour. The definition of the symbols is provided in the initial list of symbols and notations at the beginning of the paper.

Concrete type	PC	FRC50	FRC75
E [MPa]	33 500	30 800	32 100
f_{c0} [MPa]	15.5	12.8	13.2
f_{cp} [MPa]	38.7	32.1	33.1
f_{cr} [MPa]	7.7	6.4	6.6
G_c [N/mm]	35	34	34
f_t [MPa]	2	1.6	1.67
f_{Ftu} [MPa]	–	1.67	2
G_f [N/mm]	0.14	4.2	5
ν [–]	0.2	0.2	0.2
Type of bars	**E [MPa]**	**f_y [MPa]**	
⌀14	210 000	506	
⌀20	210 000	555	
⌀24	210 000	518	

by searching an equilibrium configuration at each loading step [60,61]:

$$R_t - F_t^{in} = 0 \tag{4}$$

where R_t is the vector of the external nodal forces and F_t^{in} the vector of the internal nodal forces. The approximate equilibrium solution is found using the Newton–Raphson method.

3.2. FE model

The Finite Element chosen for the beam is a 2D Shell, shown in Fig. 5. The rebars are modelled with 1d truss elements, and the corresponding sections were created with the command *Sections → Fibres*. The restrain conditions are a pin and a roller at the supports to reproduce the boundary scheme realized during the experimental tests. The dimension of mesh size for the discretization depends on the cross-section dimension to perform a correct approximation. Constraint conditions are introduced to represent the bond between concrete and reinforcement and the anchorage of bars. The constraint is obtained with a penalty approach, using a penalty stiffness value assumed equal to 1E06 in order not to allow the bar's slip and simultaneously avoid numerical instabilities. The load is distributed on a length equal to the plate width (120 mm). The load distribution is vital to avoid stress concentration under the loading zone and numerical instabilities. After a convergence analysis, the authors used a 25 mm uniform mesh.

4. Results

This section shows the results of the FE modelling of the Minelli beams using the DamageTC3d model [57]. The following parameters are selected to describe the accuracy of the FE predictions.

- P_{cr} first cracking load $P_{cr} = \frac{4 \cdot f_{ctm}}{l \cdot W}$;
- P_u Maximum capacity;
- δ Displacement corresponding to the maximum capacity;
- S_1: Slope of the first elastic phase.
- S_2 Slope of the second nonlinear phase.

The authors will first compare the experimental and numerical outcomes based on the crack pattern. Then, a quantitative assessment is provided.

4.1. Crack pattern

Fig. 6 compares the nine cases' experimental and numerical crack patterns.

The estimated crack pattern, displayed by a coloured contour plot, is compared to the experimental one shown in [51]. Moving from the left (PC) to the right (FRC75), the numerical model shows that the fibre embodiment leads to a significant increment in the number of cracks, almost uniformly distributed. Conversely, plain concrete exhibits a few wider cracks. There could be a better matching of the crack directions. In plain concrete, despite the embrittlement of the response, there are minor vertical cracks by the mid-span and a larger diagonal crack with an increasing slope as the size grows. In the simulated case, only vertical cracks start from the midspan, which becomes diagonal at a certain point following the same direction, coinciding with the large diagonal crack found experimentally. The experimental diagonal crack is like the envelope of the cracks, which rise almost vertically at the lower beam side. The numerical model seizes the size effect in plain concrete. As the size of the beam increases, the cracks have a higher slope revealing a more brittle response. Minelli et al. show that the beam's size does not significantly affect the shear capacity when using fibre reinforcement, compared to the case with plain concrete. The numerical model also confirms this aspect. The other six cases are similar, obtained with two sizes and two FRC. The cracks start like sub-diagonal by the lower beam side and then bend and converge towards the same diagonal direction, almost coinciding with the experimental one, marked in thick black. The unique parameter varied between PC, FRC50 and FRC75 is the

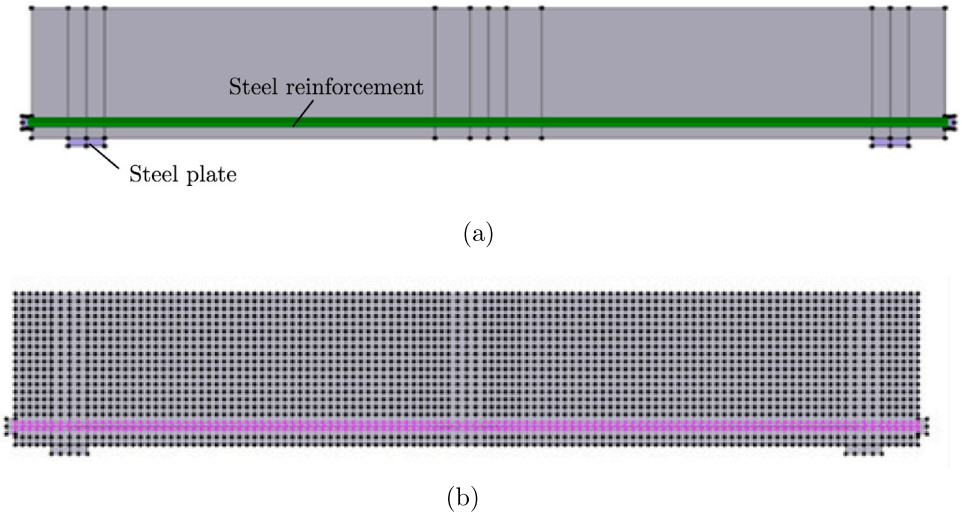

Fig. 5. (a) Beam geometry and property assignment in STKO Opensees for Minelli's beam; (b) Mesh plot for Minelli's beams in STKO Opensees.

fracture energy; see Table 2. The crushing energy is not significantly different between the three materials. Conversely, the increment of the fracture energy G_f from 0.14 (PC) to 5 (FRC75) is the cause of the observed differences among the crack patterns. The following subsections are organized based on the beam heights: H500, H1000 and H1500. The influence of geometry in fracture mechanics is well known as size effect [62], and it must be considered for high beams as the H1000 and H1500 are. This aspect makes it reasonable to investigate the G_f parameter to make the modelling more realistic. However, the f_t is also hard to measure due to the experimental difficulty of a direct concrete axial tensile test [63] and it can be affected by the size effect [64,65]. The authors found that the tensile fracture energy is the sole relevant parameter, whose variation highlight affects the beam response. Therefore, a parametric study is carried out. Each case is simulated using five values of the fracture energy, as follows:

$$\boldsymbol{G}_f = \{1.2 \cdot G_f,\ 1 \cdot G_f,\ 0.75 \cdot G_f,\ 0.5 \cdot G_f,\ 0.25 \cdot G_f\} \tag{5}$$

Then, the ultimate capacity obtained from the five curves are compared to the experimental one to estimate the relative error as a function of the G_f multiplier.

Table 3
Comparison between experimental, analytical and numerical predictions for the beams H500.

Label	P_{cr} [kN]	P_u [kN]	δ [mm]	S_1 [–]	S_2 [–]
Experimental	75	224	3.7	187	43
Numerical	41	218	3.03	197	47
Analytical	47	224	–	–	–
Numerical/Experimental	0.55	0.97	0.82	1.05	1.09
Analytical/Experimental	0.63	1	–	–	–
H500FRC50					
Experimental	35	472	23.18	197	54
Numerical	37	441	10.56	210	54
Analytical	39	394	–	–	–
Numerical/Experimental	1.06	1.07	0.46	1.07	1
Analytical/Experimental	1.11	0.83	–	–	–
H500FRC75					
Experimental	35	462	9.07	205	48
Numerical	39	441	9.6	182	57
Analytical	39	416	–	–	–
Numerical/Experimental	1.13	1.05	1.06	0.89	1.19
Analytical/Experimental	1.11	0.9	–	–	–

4.2. H500

Based on the control parameter settled as in Tables 2, 3 shows the results obtained by the analysis in terms of the selected parameters described before for the beams with H = 500 mm. The values for the fracture energy corresponding to the values reported in Table 3 are obtained with Eq. (3).

The following aspects can be observed from the inspection of Table 3 and Fig. 7.

- H500PC. There is a good agreement between experimental and simulated force–displacement curves, as shown in Fig. 7. Nonetheless, the model is not able to follow the entire experimental curve. There is an excellent agreement with the ultimate load with an error less 3%; see Table 3. The same considerations are valid for S_1 and S_2. The higher discrepancies arise for P_{cr}, approximately equal to 23%. Further discrepancies affect the stiffness evolution related to the progress of damage. The main differences in P_{cr} depend on the beam geometry, characterized by low slenderness. Therefore, the Euler–Bernoulli formulation used for predicting P_{cr} might not be entirely reliable. If the first mechanism activated is the strut and tie, the cracking process starts from a short microcrack in the tie. Afterwards, the cracks grow in height by the midspan zone due to the flexural mechanism. The crack pattern by [51] shows significant flexural cracks at 100 kN. The numerical model reaches the concrete tensile strength at 37 kN, lower than the value obtained from the EB hypothesis, see Table 3. This fact proves that the first crack is related to the tensile strength attainment in the equivalent tie. The FEM prediction does not perfectly match the stiffness evolution. The midspan cracks start growing for loads higher than 75 kN. Then, they spread horizontally, creating a smoother stiffness loss; see Fig. 7. Nonetheless, despite the observed differences, the failure load is almost identical, proving the FE model's accuracy.
- H500FRC50: The experimental curve in Fig. 7(b) shows a linear trend up to 50 kN. Then, there is a significant stiffness loss up to the bars' yielding, followed by a plateau until failure. Fig. 7 shows the crack pattern corresponding to failure. The fibre contribution to the response manifests in the post-cracking phase after 50 kN. This part is associated with dense damage spreading. The numerical model before optimization closely seizes the pre-yielding phase, while it struggles in following the post-yielding stage. The steel fibres contribution governs the post-crack behaviour. Table 3 reveals a good agreement between experiment and simulation for P_u, S_1 and S_2, with a maximum error equal to 7%. The major

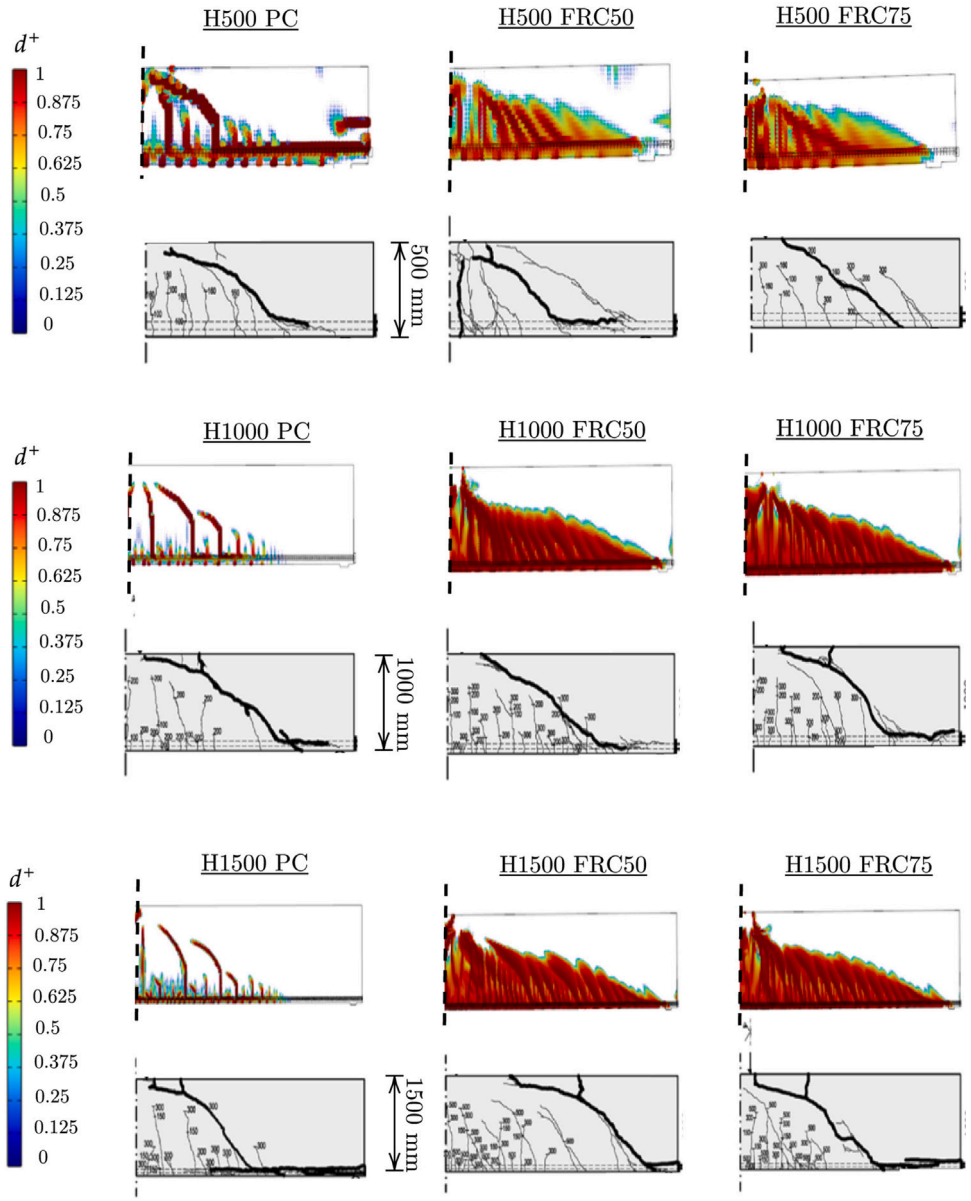

Fig. 6. Comparison between all cases numerical and experimental crack patterns. (For interpretation of the references to colour in this figure legend, the reader is referred to the web version of this article.)

differences occur for the ultimate displacement predictions. Compared to the plain concrete beams, it is challenging to graphically observe P_{cr} from the curve since the stiffness change associated with the first crack is not manifest. Nonetheless, there is also a good matching for P_{cr}, as revealed by the results in Table 3. The crack pattern in Fig. 7 shows a precise shear-flexural mechanism with diagonal and vertical cracks.

- H500FRC75: The experimental curve shows a linear trend up to 53 kN, followed by a nonlinear stage until the failure. The numerical curve before optimization shows a good agreement with the experimental one. The beam slenderness affects the beam sensitivity to the value of the fracture energy, as later discussed. Therefore, it is expected to observe a better improvement in the prediction for deeper beams after optimization. Interestingly, the numerical curve shows a softening behaviour not reported by the experimental results. The parameters obtained by the analysis in Table 3 exhibits a good agreement in terms of P_u, S_1 and δ with a maximum error equal to 11%. The slope of the nonlinear part (S_2) has a higher error, 19%. The failure crack pattern corresponds to a shear mechanism. Nonetheless, the extent of the crack pattern of the model is lower than the experimental one, as evidenced in Fig. 7.

The results show that the expression of the fracture energy and the input parameters lead to a good agreement in terms of failure load. The main differences arise in the first cracking stages, also related to possible different initial conditionals between the model and the tested beams, and the ultimate displacement.

Fig. 7 also shows the dependence of the model predictions on the input fracture energy. While in the case of plain concrete (see Fig. 7(a)), a variation in the fracture energy leads to a higher discrepancy, the differences reduce when considering a fibre-reinforced specimen (see Fig. 7(b)–(c)). The high sensitivity detected in plain concrete with respect to the different values of G_f can be considered as a clear evidence of the uncertainties in the mix-design procedure adopted for the specimen casting. As a matter of fact, by introducing the fibres in the specimen volume, the variation between the different curves in Fig. 7(b)–(c) becomes less evident due to the effective mechanical

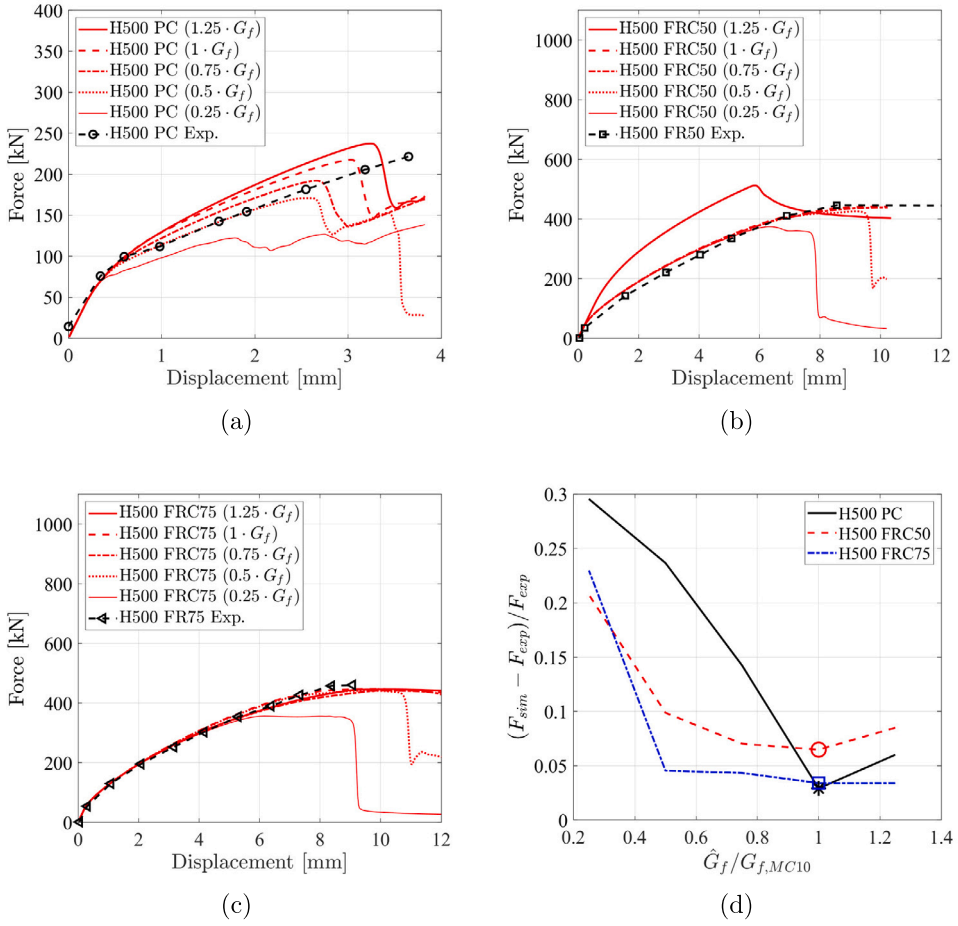

Fig. 7. Comparison between numerical and experimental force–displacement curves for the beams H500. (a), (b) and (c) refer to PC, FRC50 and FRC75 beams, respectively. (d) shows the relative error as a function of the fracture energy multiplier.

properties of the fibres. In this way, the uncertainties that characterize plain concrete gradually vanish due to the increase in fibre content. Moreover, the fact might be related to the reference value of the G_f calculated according to Eq. (3), which is much lower in plain concrete and higher for the fibre-reinforced case (see Table 2). By multiplying an amplification or reduction factor to G_f (see (5)), a further reduction of an already small G_f leads to significant embrittlement of the response with related capacity and ductility reduction. Conversely, in fibre-reinforced, the curves appear almost independent of the input fracture energy when it varied between maximum and minimum value of the chosen range of G_f. A major discrepancy arises in Fig. 7(b), when a 1.25 multiplier is used, leading to a consistent overestimation of the beam response. Although plain concrete has a higher sensitivity to the fracture energy multiplier, the best agreement in terms of the ultimate load is achieved with $\hat{G}_f = 1 \cdot G_f$. This fact proves that the expression in Eq. (3) can be considered valid for both PC and FRC in the smallest specimen with H = 500 mm and L = 2640 mm.

4.3. H1000

This subsection present and discusses the predictions for the H1000 beam responses using the value for the fracture energy suggested by the MC2010 and the optimized one. Table 4 pointed out the values used to compare the experimental, numerical and analytical predictions. The values in Table 4 correspond to the fracture energy multipliers equal to one. Fig. 8 plots the experimental and simulated force–displacement curves with the considered values of the fracture energy.

The main aspects arising from the analysis of Fig. 8, Table 4 and the crack patterns before G_f optimization are:

Table 4
Comparison between experimental, analytical and numerical predictions for FR50 beams.

Label	P_{cr} [kN]	P_u [kN]	δ [mm]	S_1 [–]	S_2 [–]
H1000PC					
Experimental	100	340	6.3	179	42
Numerical	77	323	4.86	190	43
Analytical	88	393	–	–	–
Numerical/Experimental	0.77	0.95	0.77	1.06	1.02
Analytical/Experimental	0.88	1.16	–	–	–
H1000FRC50					
Experimental	41	528	11.68	187	55
Numerical	71	818	17.83	179	40
Analytical	70	722	–	–	–
Numerical/Experimental	1.73	0.64	1.53	0.96	0.73
Analytical/Experimental	1.71	1.37	–	–	–
H1000FRC75					
Experimental	67	686	14.31	147	40
Numerical	71	824	17.1	186	46
Analytical	70	762	–	–	–
Numerical/Experimental	1.06	0.83	1.2	1.26	1.15
Analytical/Experimental	1.04	1.11	–	–	–

- H1000PC. The same considerations highlighted for the H500 PC beam are valid for the H1000PC one. The experimental curve in Fig. 8(a) shows a manifest change of stiffness at 100 kN. As observed with the H500PC, the first crack load evaluated with Bernoulli's theory is lower, close to 88 kN. The numerical

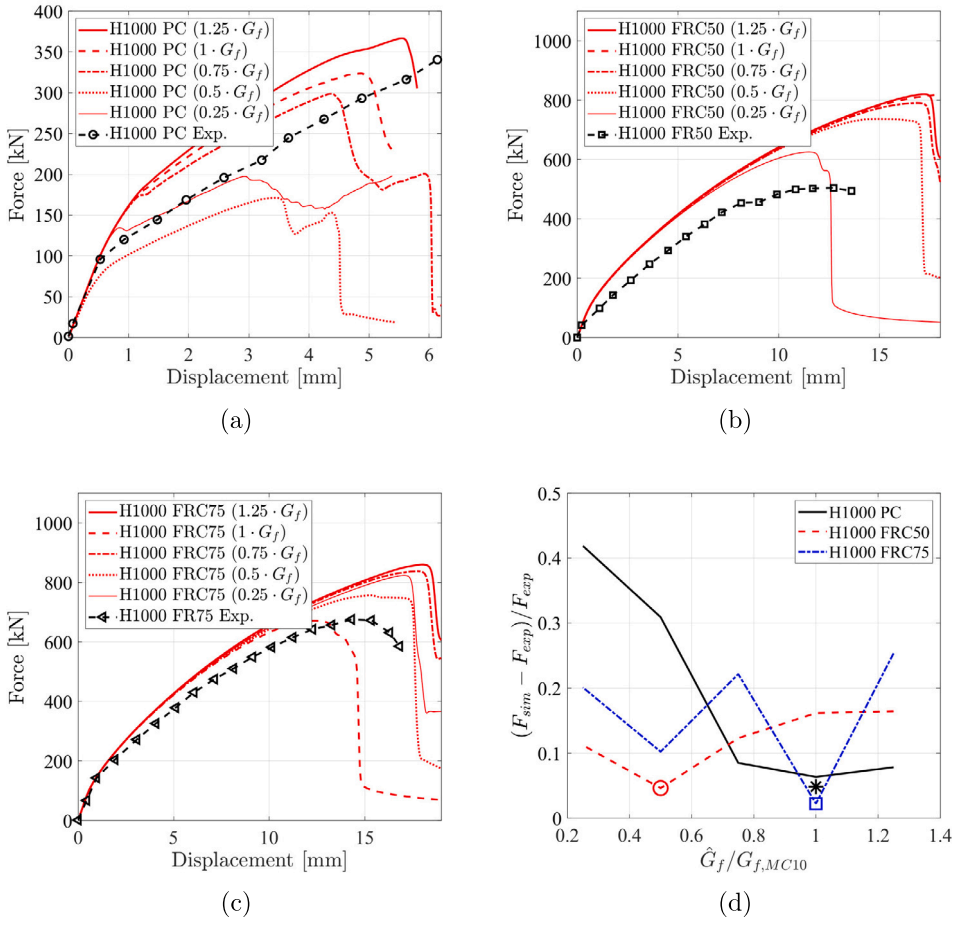

Fig. 8. Comparison between numerical and experimental force–displacement curves of the FR50 specimens. (a), (b) and (c) refer to PC, FRC50 and FRC75 beams, respectively. (d) shows the relative error as a function of the fracture energy multiplier.

curve exhibits the first crack at 77 kN, corresponding to a tensile strength equal to 2 MPa in the bottom part. The lower the slenderness, the higher the model's difficulty closely mirroring the crack pattern. The error for P_{cr} and δ is approximately 23%. Additionally, S_1 and S_2 are in good agreement with an error lower than 6% and 2%, respectively. The main discrepancy in the crack pattern is the lower height of the flexural cracks in the numerical model. The failure load is almost identical for the H500 PC beam.

- H1000FRC50: Minelli et al. observed that this beam exhibited a lower shear capacity contrary to expectations. This fact might be the reason for the overestimation of the capacity by the numerical model. This discrepancy occurs for almost all control parameters, as shown in Table 4. The experimental crack pattern, in Fig. 6, is not related to shear failure, being governed by an almost vertical crack. Given the excellent agreement with the experimental results for H500 FR50, it is likely that the experimental beams have initial cracking patterns that biased the final capacity estimate, leading to a more fragile observed response. Moreover, the experimental curve shows a rapid strength decay, possibly caused by a cracked state before the tests. The sample's integrity heavily influences the possible underestimation of load capacity before the test, i.e. the crack propagation can be accelerated by the presence of the crack.
- H1000FRC75: The experimental curve is linear up to 104 kN. The numerical curve is close to the experimental one, but as for H500FR75, it has a higher stiffness. As observed for the H1000FRC50, the ultimate load presents a significant error, approximately equal to 12%. Therefore, the same considerations for H1000FR50 can be considered valid for this case study.

There is a lower sensitivity in FRC to G_f. The optimum multiplier for H1000FRC75 equals one, while it lowers to 0.5 in the H1000FRC50 case. Despite occurring in the sole H1000FRC50 case, the analyses reveal a size effect in the optimal fracture energy for FRC specimens. A larger size does not allow fully exploiting the potential fracture energy obtained from Eq. (3), which should be reduced. This aspect will be more evident in the H1500 case.

4.4. H1500

This subsection present and discusses the predictions for the H1500 beam responses using the value for the fracture energy suggested by the MC2010 and the optimized one. Table 5 resumes the values derived by the analysis used to compare the experimental, numerical and analytical predictions. The values in Table 5 correspond to the fracture energy multipliers equal to one. Fig. 9 plots the experimental and simulated force–displacement curves with the considered values of the fracture energy. The main aspects arising from the analysis of Fig. 9, Table 5 and the crack patterns in Fig. 6 before G_f optimization are:

- The H1500PC experimental curve in Fig. 9(a) has a linear branch up to 60 kN, lower than the first crack load P_{cr} estimated with the Euler–Bernoulli theory equal to 130 kN. The numerical curve shows a higher discrepancy to the experimental one, with a P_{cr} error of 300% and a displacement difference close to 24%. This might depend on a possible cracking pattern of the experimental beam before testing. The numerical model shows that the first crack appears at 150 kN with tensile stress equal to 2.2 MPa.

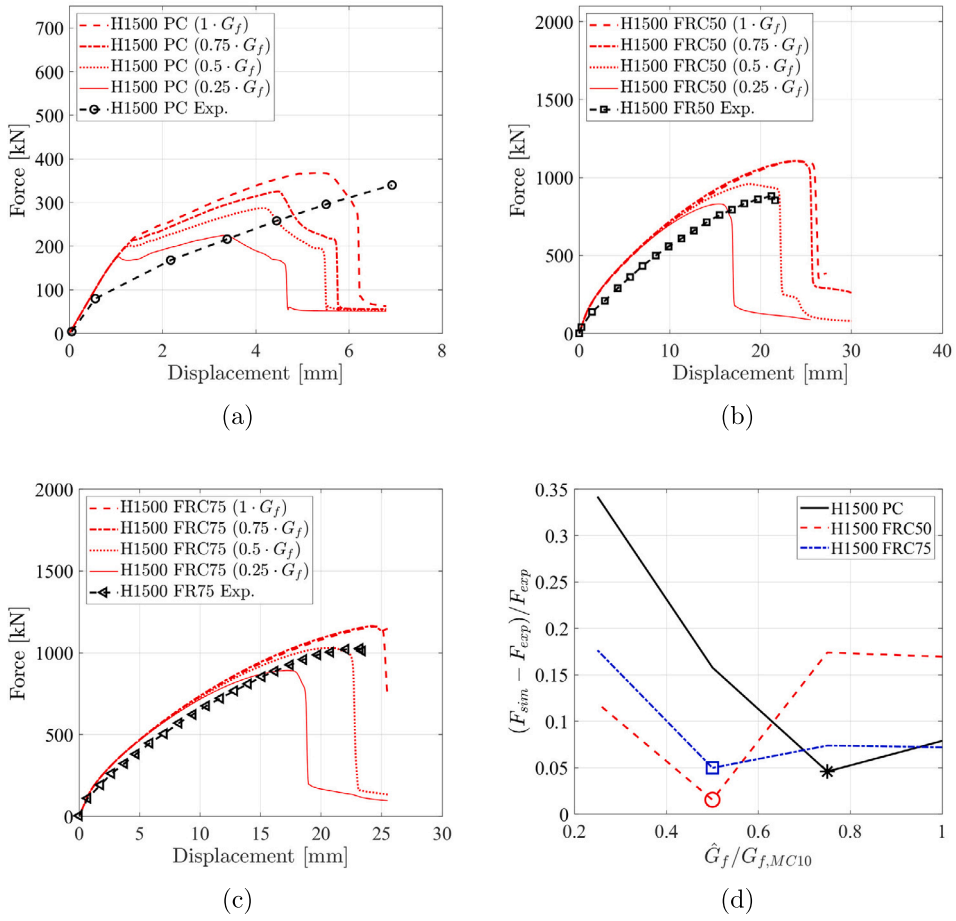

Fig. 9. Comparison between numerical and experimental force–displacement curves of the FR75 specimens. (a), (b) and (c) refer to PC, FRC50 and FRC75 beams, respectively. (d) shows the relative error as a function of the fracture energy multiplier.

Table 5
Comparison between experimental, analytical and numerical estimations for FR75 beams.

Label	P_{cr} [kN]	P_u [kN]	δ [mm]	S_1 [–]	S_2 [–]
H1500PC					
Experimental	50	341	7	209	39
Numerical	150	368	5.35	179	43
Analytical	130	523	–	–	–
Numerical/Experimental	3	1.08	0.76	0.86	1.1
Analytical/Experimental	2.6	1.53	–	–	–
H1500FRC50					
Experimental	39	943	21.18	158	38
Numerical	101	1103	21.18	164	43
Analytical	104	1019	–	–	–
Numerical/Experimental	2.59	0.86	1	1.04	1.13
Analytical/Experimental	2.67	1.08	–	–	–
H1500FRC75					
Experimental	111	1083	23.2	151	45
Numerical	101	1103	24.65	176	42
Analytical	104	1073	–	–	–
Numerical/Experimental	0.91	0.98	1.06	1.16	0.93
Analytical/Experimental	0.94	0.99	–	–	–

Likely, the first activated mechanism is the arch rather than the flexural one. The experimental crack propagation has been faster than the numerical due to the high stiffness loss observed in the experimental curve. Nonetheless, the stiffness up to failure is quite similar, and the final crack pattern resembles the actual one, as shown in Fig. 6. Additionally, the error in terms of the ultimate load is minimal, with an 8% error.

- H1500FRC50: The predictions for the H1500FRC50 are better than the previous case. The numerical curve closely follows the pre-cracking response, despite showing a stiffer response in the nonlinear stage. There is a 12% error in the ultimate load prediction, higher than the error value obtained from previous cases. There is a good agreement with the final crack pattern, although the crack localization is quite shifted compared to the experimental evidence.
- H1500FRC75: The experimental curve is linear up to 111 kN, reaching failure at 1161 kN. The numerical curve closely follows the experimental one, although with higher stiffness, see Fig. 9(c). The same considerations for H1000FR50 can be considered valid for this case study.

As observed for H500 and H1000, also in the current case study the PC beams show a higher sensitivity to the G_f multiplier. Despite the difficulty in closely following the experimental curve, the optimal capacity is obtained with a G_f multiplier equal to 0.75. In the other two cases, there is still a low sensitivity to the G_f multiplier compared to PC. The optimal matching is achieved with the two multipliers equal to 0.5. The size increment of the beam leads to a reduction of the optimal fracture energy in both PC and FRC. This observation confirms the findings of H1000. A larger beam size does not allow to exploit the fracture energy predicted by Eq. (3) fully. Therefore, G_f must be reduced. The entity of this reduction rises when considering FRC beams.

The PC specimens exhibit the highest discrepancy between numerical and experimental curves, specifically the P_{cr} value. Likely, these

discrepancies arise from experimental uncertainties, possibly related to cracking patterns that occurred during the curing phases.

5. Discussion

Within the scientific advancements in Structural Engineering, it has been realized that the classical concept of strength, understood as force per unit surface causing failure, needs revision, especially in cases where particularly large or tiny structures are involved. The strength of the material must be compared against other characteristics, such as the toughness in the fracturing processes, to define, via the structural size, the ductility or the brittleness of the structure [66]. Two intrinsic characteristics of the material, plus a geometrical characteristic of the structure, represent the minimum basis for predicting the type of structural response. Since structures are prevalently subjected to compressive forces, a transition can be detected from plastic collapse to buckling instability as slenderness increases, so in systems subjected to tensile forces, there is a transition from plastic collapse to brittle fracture as the size-scale increases. In this framework, different numerical vs experimental investigations carried out so far [15,17,67] indicate that the flexural performance of FRC specimens is affected by: (i) the fibre volume fraction; (ii) the mechanical and geometrical properties of the reinforcing fibres (tensile strength, geometric profile, and aspect ratio) and the cementitious matrix; (iii) the specimen size. In the latter case, increasing the specimen size can detect a systematic decrease in the composite flexural strength. This geometric effect, which can also be related to the fibre distribution within the volume of the composite [17], can be quantitatively evaluated in the framework of Fracture Mechanics by using the Multi-fractal Scaling Law (MFSL) for initially uncracked specimens [68] or the Size Effect Law (SEL) for initially cracked specimens [69]. These best-fitting laws can be used to determine the size-scale effects on material mechanical parameters. On the contrary, when the global structural behaviour is function not only of material strength and toughness but also of the quantity of reinforcement together with the scale, a different approach based on Dimensional Analysis is needed [66,70]. In particular, the scale-dependent post-cracking regimes in the structural response of steel-bar reinforced or fibre-reinforced concrete structures can be thoroughly predicted by the so-called Reinforcement Brittleness Number [15,17,67,70–72], which is a function of the reinforcement percentage, ρ, the generalized reinforcement strength, σ_s, the concrete fracture toughness, K_{IC}, and the structural scale, h.

$$N_P = \rho \frac{\sigma_s}{K_{IC}} \sqrt{h} \tag{6}$$

It is worth noting that the concrete generalized toughness, K_{IC}, can be evaluated following Irwin's Theorem [73]:

$$K_{IC} = \sqrt{G_f E} \tag{7}$$

In the cases under investigation, the MFSL and SEL best-fitting laws may present shortcomings in assessing size scale effects on the concrete mechanical parameters due to different reinforcement percentages, steel bars and fibres. In this framework, the abovementioned Dimensional Analysis approach can result in a more thorough and accurate determination of scale effects on global structural brittleness.

In particular, adopting a longitudinal steel-bar reinforcement for each testing specimen does not lead to a correct evaluation of the size-scale effect on the concrete matrix strength and toughness. As it is shown by a comparison between 7(d), 8(d), and 9(d), the beneficial effect provided by the fibre content concerning the plain concrete cannot be recognized. However, the adopted DamageTC3d model seems to be able to detect a variation in concrete toughness with specific regard to each material type and by varying the specimen size. The variation in the optimal fracture energy coefficient, which guarantees the best fitting between experimental and numerical curves, passes from 1 to approximately 0.75 for normal concrete, and from 1 to 0.5 for FRC, showing in any case an inverse trend concerning the well-established fractal scaling [64].

Table 6
Comparison between experimental, numerical and analytical shear capacity.

Minelli's beams	H500 FRC50	H1000 FRC50	H1500 FRC50	H500 FRC75	H1000 FRC75	H1500 FRC75
$V_{u,\exp}$ [kN]	236	264	472	231	343	542
V_{MC2010} [kN]	201	369	520	212	389	547
$V_{EC2\text{-}draft}$ [kN]	194	400	601	228	472	712
V_{num} [kN]	221	409	552	223	412	581
$V_{MC2010}/V_{u,\exp}$	0.85	1.4	1.1	0.92	1.13	1.01
$V_{EC2\text{-}draft}/V_{u,\exp}$	0.82	1.51	1.28	0.99	1.38	1.32
$V_{num}/V_{u,\exp}$	0.93	1.55	1.17	0.97	1.2	1.07

In this framework, it is worth recalling that fractal scaling represents an effective tool for assessing the size-scale dependence of critical stresses, which are not defined concerning canonical physical dimensions, but on fractal sets presenting noninteger dimensions [64,68]:

$$\sigma_u = \sigma_u^* h^{-d_\sigma} \tag{8}$$

where σ_u is the nominal stress, σ_u^* is the renormalized scale-independent stress, and $-d_\sigma$ represents the dimensional decrement. There is a general agreement that the main reason for size effect on shear stress in RC members without transverse reinforcement is the larger diagonal crack width in deeper beams. However, there is more disagreement about the correct modelling of this phenomenon. The experimental tests conducted by Minelli et al. prove that the ultimate shear stress is substantially independent of the beam size for FRC compared to the PC cases. The beam modelling using the damadeTC3d model can closely mirror the size effect in plain concrete. A larger beam size leads to wider cracks in the FE model and, accordingly, to lower ultimate shear stress. Conversely, a larger beam in FRC beams does not lead to wider cracks due to the fibre bridging action, thus mitigating the eventual size effect in shear. It is worth noting that finite element analyses based on the strength criterion usually do not yield any size effect. This paper has no ambition of delivering empirical regressions or generalized formulations for predicting the size-scale dependence of shear strength and toughness in FRC. This task would entail dedicated efforts based on a more extended experimental campaign focused on size-scale effects in the FRC beams shear response. On the contrary, this work highlights the crucial importance of size-scale effects in modelling FRC beams based on a specific case study and concerning nonlinear fracture mechanics modelling.

6. Comparison between numerical, experimental and analytical predictions

This section compares the experimental capacity versus the FE and analytical formulations. Two analytical formulations are used, resumed in the following synoptic table, the one in the MC2010 and the EC2 draft [74] for FRC. The synoptic table's detailed list of symbols used is provided in the initial list of symbols and notation.

The MC2010 formulation assumes that the fibres provide a distributed reinforcement. The shear contribution of fibres is modelled as a function of the longitudinal displacement ratio. The new EC2 draft proposes another formulation considering the relation between the aggregate size and the effective depth. For the prestressed element, the term 0.15 σ_{CP} is added to $\tau_{Rd,cf}$.

Analytical formulations for the shear capacity for FRC

MC2010 [51]

- $V_u = \{\frac{0.18}{\gamma_c} \cdot k[100 \cdot \rho_l(1+7.5 \cdot \frac{f_{Ftuk}}{f_{ctk}} \cdot f_{ck})]^{\frac{1}{3}} + 0.15\sigma_{cp}\} \cdot b_w \cdot d$

New EC2 draft proposal

- $V_u = \tau_{Rd,cf} \cdot b_w \cdot z$
- $\tau_{Rd,cf} = \eta \frac{0.6}{\gamma_c}(100 \cdot \rho_l \cdot f_{ck} \cdot \frac{d_{dg}}{d})^{\frac{1}{3}} + f_{Ftud} > \eta \cdot \tau_{Rd,cmin} + f_{Ftud}$
- $f_{Ftud} = \frac{f_{Ftuk}}{\gamma_F}$
- $\eta = \max(\frac{1}{1+0.43 \cdot f_{Ftuk}}; 0.4)$
- $d_{dg} = \{16 + D_{lower} \leq 40\ [\text{mm}]\}$ if
  - (a) $f_{ck} \leq 60\ [\text{MPa}] \cdot 16 + D_{lower}(\frac{60\ [\text{MPa}]}{f_{ck}})^2 \leq 40\ [\text{mm}]$
  - (b) $f_{ck} > 60\ [\text{MPa}]$
- $\tau_{Rd,min} = \frac{11}{\gamma_v} \cdot \sqrt{\frac{f_{ck} \cdot d_{dg}}{f_{yd}}} \cdot d$

Table 6 compares the shear capacity according to the MC2010 formulation, the EC2 draft [74] and the FE model. Tables 7 and 8 list all the input parameters used in the analytical formulations. The accuracy of the three models is comparable in all cases. Interestingly, the accuracy does not substantially depend on the model selection but on the specimen under analysis. Some specimens, like H500, exhibit good accuracy, with a relative error lower than 10%. In some cases, like H1000 FRC50, the models significantly overestimate the experimental capacity. However, in general, the three models are nonconservative, except for H500, where the models predict lower values of the shear capacity.

The analysis of Table 6 reveals that the FE predictions exhibit similar accuracy to the analytical models. Therefore, the unsatisfactory predictions of the FE model do not depend on modelling flaws but on the material and experimental uncertainty. The worst performance is obtained with the EC2 draft, which slightly overestimates the shear capacity. The three models do not consider any uncertainty, which might cause error discrepancies between the nine cases.

7. Conclusions

This paper addresses the size-scale effect issue in the numerical modelling of fibre-reinforced concrete beams using the DamageTC3d model in STKO Opensees. The beams tested by Minelli et al. [51] is used as a benchmark case study to investigate the modelling issues of FRC. The analyses reveal that the optimum agreement between the experimental and the numerical estimates is obtained by varying the fracture energy G_f as the beam size grows. Concerning the ultimate capacity, the analytical and the numerical models are, on average, nonconservative, with a mean relative error reaching 50% in a few cases, while in general is less than 10%.

The paper focuses on specific case studies and does not provide empirical regressions useful for correctly choosing the G_f value for predicting the shear capacity of large-size beams. Nevertheless, this work emphasizes the role of fracture energy in correctly estimating the FRC beam response using the DamageTC3d model implemented in Opensees STKO. The comparison between the numerical estimates and the analytical predictions using the MC2010 and the current EC2 draft proves that the error is substantially independent of the model selection. Still, it is highly affected by the specific case study. This fact confirms the absence of flaws in the numerical modelling but highlights the high uncertainties related to the estimates not included in the analyses. Finally, since damage, strain localization, and fracture are phenomena not always interpretable in the framework of Continuum Mechanics, the practical tools offered by Fracture Mechanics and, in particular, by Dimensional Analysis and Fractal Geometry, can quantitatively solve the structural problem of size-scale effects. In future works, a Nonlinear Fracture Mechanics approach will be applied to investigate the flexural and shear behaviour of FRC beams, together with a more extended experimental campaign focused on size-scale effects in the FRC shear response.

Table 7
Input parameters of the MC2010 formulation in the synoptic table.

Parameter	H500 FRC50	H1000 FRC50	H1500 FRC50	H500 FRC75	H1000 FRC75	H1500 FRC75
γ_c [–]	1	1	1	1	1	1
d [mm]	440	940	1440	440	940	1440
k [–]	1.67	1.46	1.37	1.67	1.46	1.37
ρ_l [–]	0.0112	0.0107	0.01	0.0112	0.0107	0.01
f_{Ftuk} [MPa]	1.67	1.67	1.67	2.01	2.01	2.01
f_{ctm} [MPa]	2.4	2.4	2.4	2.5	2.5	2.5
f_{cm} [MPa]	32.1	32.1	32.1	33.1	33.1	33.1
b_w [mm]	250	250	250	250	250	250
$V_{u,\text{MC2010}}$ [N]	201 194	369 488	519 852	211 742	388 859	547 106

CRediT authorship contribution statement

Raffaele Cucuzza: Conceptualization, Methodology, Validation, Formal analysis, Investigation, Data curation, Writing – original draft, Writing & editing, Visualization, Supervision. **Angelo Aloisio:** Conceptualization, Methodology, Validation, Formal analysis, Investigation, Data curation, Writing – original draft, Writing & editing, Visualization, Supervision. **Federico Accornero:** Investigation, Data curation, Writing – original draft, Writing & editing, Supervision. **Antonella Marinelli:** Formal analysis, Investigation, Resources, Data curation, Writing – original draft, Writing & editing. **Elisa Bassoli:** Writing & editing, Visualization, Supervision. **Giuseppe Carlo Marano:** Conceptualization, Methodology, Validation, Formal analysis, Investigation, Resources, Data curation, Writing – original draft, Writing & editing, Visualization, Supervision.

Declaration of competing interest

The authors declare that they have no known competing financial interests or personal relationships that could have appeared to influence the work reported in this paper.

Data availability

Data will be made available on request.

Acknowledgements

The authors kindly acknowledge the contribution given by Guido Camata and Massimo Petracca for the academic license of STKO software and for the fundamental support in developing the present work.

Appendix

See Tables 7 and 8.

Table 8
Input parameters of the EC2 draft formulation in the synoptic table.

Minelli's beams	H500 FRC50	H1000 FRC50	H1500 FRC50	H500 FRC75	H1000 FRC75	H1500 FRC75
γ_C [–]	1	1	1	1	1	1
γ_F [–]	1	1	1	1	1	1
γ_V [–]	1	1	1	1	1	1
d [mm]	440	940	1440	440	940	1440
z [mm]	396	846	1296	396	846	1296
ρ_l [–]	0.0112	0.0107	0.01	0.0112	0.0107	0.01
f_{yd} [MPa]	440	440	440	440	440	440
f_{Ftuk} [MPa]	1.67	1.67	1.67	2.01	2.01	2.01
f_{Ftud} [MPa]	1.67	1.67	1.67	2.01	2.01	2.01
f_{ctm} [MPa]	2.4	2.4	2.4	2.5	2.5	2.5
f_{cm} [MPa]	32.1	32.1	32.1	33.1	33.1	33.1
D [mm]	5	5	5	5	5	5
d_{dg} [mm]	21	21	21	21	21	21
b_w [mm]	250	250	250	250	250	250
η [–]	0.4	0.4	0.4	0.4	0.4	0.4
$\tau_{Rd,c,min}$ [MPa]	0.18	0.12	0.1	0.18	0.12	0.1
$\tau_{Rd,cf}$ [MPa]	1.96	1.89	1.86	2.3	2.23	2.2
$\eta_{\tau Rd,c,min}$ + fFtud [MPa]	1.74	1.72	1.71	2.08	2.06	2.05
$V_{u,\mathrm{EC2\text{-}draft}}$ [N]	193 775	399 676	601 458	227 728	472 064	712 238

References

[1] Z. Yu, Q. Huang, X. Xie, N. Xiao, Experimental study and failure criterion analysis of plain concrete under combined compression-shear stress, Constr. Build. Mater. 179 (2018) 198–206.
[2] A. Neville, P.-C. Aitcin, High performance concrete—An overview, Mater. Struct. 31 (2) (1998) 111–117.
[3] B. Graybeal, Ultra-High Performance Concrete, Tech. Rep., 2011.
[4] V. Afroughsabet, L. Biolzi, T. Ozbakkaloglu, High-performance fiber-reinforced concrete: a review, J. Mater. Sci. 51 (14) (2016) 6517–6551.
[5] D.-Y. Yoo, Y.-S. Yoon, Structural performance of ultra-high-performance concrete beams with different steel fibers, Eng. Struct. 102 (2015) 409–423.
[6] F.I. Du Béton, Fib Model Code for Concrete Structures 2010, Wiley-vch Verlag Gmbh, 2013.
[7] C. Européen, Eurocode 2: Design of Concrete Structures—Part 1-1: General Rules and Rules for Buildings, British Standard Institution, London, 2004.
[8] N. Afnor, K. Droll, P18-710: National Addition to Eurocode 2–Design of Concrete Structures: Specific Rules for Ultra-High Performance Fiber-Reinforced Concrete (UHPFRC), Association Française de Normalisation, 2016.
[9] S. CT, 2052: Béton Fibré Ultra-Performant (BFUP)-Matériaux, Dimensionnement et Exécution, Société Suisse des Ingénieurs et Architectes, Zürich, 2015.
[10] ASTM, Annual Book of ASTM Standards, 1990: Subject Index; Alphanumeric List, American Society for Testing & Materials, 1990.
[11] J. Recommendations, Japan society of civil engineers (JSCE): Recommendations for design and construction of ultra-high strength fiber-reinforced conerete structures, JSCE Guidel. Concr. (9) (2006).
[12] S.H. Ahmad, C.H. Henager Sr, M. Arockiasamy, P. Balaguru, C. Ball, H.P. Ball Jr., G.B. Batson, A. Bentur, R.J. Craig, M.E. Criswell, et al., Design considerations for steel fiber reinforced concrete, 1988.
[13] M. Di Prisco, M. Colombo, D. Dozio, Fibre-reinforced concrete in fib model code 2010: principles, models and test validation, Struct. Concr. 14 (4) (2013) 342–361.
[14] I. Löfgren, Fibre-Reinforced Concrete for Industrial Construction, Chalmers, Göteborg, 2005.
[15] F. Accornero, A. Rubino, A. Carpinteri, Post-cracking regimes in the flexural behaviour of fibre-reinforced concrete beams, Int. J. Solids Struct. 248 (2022) 111637.
[16] F. Accornero, A. Rubino, A. Carpinteri, Ultra-low cycle fatigue (ULCF) in fibre-reinforced concrete beams, Theor. Appl. Fract. Mech. 120 (2022) 103392.
[17] A. Carpinteri, F. Accornero, A. Rubino, Scale effects in the post-cracking behaviour of fibre-reinforced concrete beams, Int. J. Fract. (2022) http://dx.doi.org/10.1007/s10704--022--00671--x.
[18] P. Vaishnav, A. Titiksh, Evaluating the performance of hybrid fibre reinforced self compacted concrete (hfrscc) using steel and banana fibres, J. Ceram. Concr. Sci. 1 (1) (2016) 1–10.
[19] K. Gharehbaghi, Advancements in concrete technology in Australia: Geo-polymer concrete., Int. J. Constr. Environ. 7 (1) (2015).
[20] F. Liu, W. Ding, Y. Qiao, Experimental investigation on the tensile behavior of hybrid steel-PVA fiber reinforced concrete containing fly ash and slag powder, Constr. Build. Mater. 241 (2020) 118000.
[21] S.-H. Chao, J.-S. Cho, N.B. Karki, D.R. Sahoo, N. Yazdani, FRC performance comparison: uniaxial direct tensile test, third-point bending test, and round panel test, Spec. Publ. 276 (2011) 1–20.
[22] M. Di Prisco, G. Plizzari, L. Vandewalle, Structural design according to fib MC 2010: comparison between RC and FRC elements, Proc. FRC (2014) 69–87.
[23] L. Rizzuti, F. Bencardino, Effects of fibre volume fraction on the compressive and flexural experimental behaviour of SFRC, Contemp. Eng. Sci. 7 (8) (2014) 379–390.
[24] F. Bencardino, L. Rizzuti, G. Spadea, R.N. Swamy, Stress-strain behavior of steel fiber-reinforced concrete in compression, J. Mater. Civ. Eng. 20 (3) (2008) 255–263.
[25] J.D. Blunt, C.P. Ostertag, Deflection hardening and workability of hybrid fiber composites, ACI Mater. J. 106 (3) (2009) 265.
[26] D.M. Moreno, W. Trono, G. Jen, C. Ostertag, S.L. Billington, Tension stiffening in reinforced high performance fiber reinforced cement-based composites, Cem. Concr. Compos. 50 (2014) 36–46.
[27] R.F. Zollo, Fiber-reinforced concrete: an overview after 30 years of development, Cem. Concr. Compos. 19 (2) (1997) 107–122.
[28] N. Banthia, Fiber Reinforced Concrete, ACI SP-142ACI, Detroit, MI 91, 1994, p. 119.
[29] A. Conforti, F. Minelli, G.A. Plizzari, G. Tiberti, Comparing test methods for the mechanical characterization of fiber reinforced concrete, Struct. Concr. 19 (3) (2018) 656–669.
[30] A.F. Pour, T. Ozbakkaloglu, T. Vincent, Axial compressive behavior of ultra-high-strength steel fiber-reinforced concrete-filled fiber reinforced polymer (FRP) tube columns, Compos. Struct. 266 (2021) 113777.
[31] Z. Sun, Y. Yang, W. Qin, S. Ren, G. Wu, Experimental study on flexural behavior of concrete beams reinforced by steel-fiber reinforced polymer composite bars, J. Reinf. Plast. Compos. 31 (24) (2012) 1737–1745.
[32] R. Olivito, F. Zuccarello, An experimental study on the tensile strength of steel fiber reinforced concrete, Composites B 41 (3) (2010) 246–255.
[33] X. Wang, F. Fan, J. Lai, Y. Xie, Steel fiber reinforced concrete: A review of its material properties and usage in tunnel lining, in: Structures, Vol. 34, Elsevier, 2021, pp. 1080–1098.
[34] A.A. Shah, Y. Ribakov, Recent trends in steel fibered high-strength concrete, Mater. Des. 32 (8–9) (2011) 4122–4151.
[35] A. Hillerborg, M. Modéer, P.-E. Petersson, Analysis of crack formation and crack growth in concrete by means of fracture mechanics and finite elements, Cem. Concr. Res. 6 (6) (1976) 773–781.
[36] J.C. Walraven, High performance fiber reinforced concrete: progress in knowledge and design codes, Mater. Struct. 42 (9) (2009) 1247–1260.
[37] H. Singh, Steel Fiber Reinforced Concrete: Behavior, Modelling and Design, Springer, 2016.
[38] W. Abbass, M.I. Khan, S. Mourad, Evaluation of mechanical properties of steel fiber reinforced concrete with different strengths of concrete, Constr. Build. Mater. 168 (2018) 556–569.
[39] J.-H. Lee, B. Cho, E. Choi, Flexural capacity of fiber reinforced concrete with a consideration of concrete strength and fiber content, Constr. Build. Mater. 138 (2017) 222–231.
[40] V.K. Kytinou, C.E. Chalioris, C. G. Karayannis, Analysis of residual flexural stiffness of steel fiber-reinforced concrete beams with steel reinforcement, Materials 13 (12) (2020) 2698.
[41] V.S. Gopalaratnam, S.P. Shah, G. Batson, M. Criswell, V. Ramakishnan, M. Wecharatana, Fracture toughness of fiber reinforced concrete, Mater. J. 88 (4) (1991) 339–353.
[42] A. Barros, J. Sena, J. Cruz, Fracture energy of steel fiber-reinforced concrete, Mech. Compos. Mater. Struct. 8 (1) (2001) 29–45.
[43] J.A. Barros, J.A. Figueiras, Experimental behaviour of fibre concrete slabs on soil, Mech. Cohes. Frict. Mater.: Int. J. Exp. Model. Comput. Mater. Struct. 3 (3) (1998) 277–290.
[44] J.A. Barros, Experimental behavior of mesh reinforced shotcrete and steel fiber reinforced shotcrete panels, 1998.
[45] P. JSCE-SF4 III, Method of Tests for Steel Fiber Reinforced Concrete, Concrete Library of JSCE, the Japan Society of Civil Engineers, 1984.
[46] A. Hillerborg, Analysis of fracture by means of the fictitious crack model, particularly for fibre reinforced concrete, 1980.
[47] J.A. Barros, V.M. Cunha, A.F. Ribeiro, J. Antunes, Post-cracking behaviour of steel fibre reinforced concrete, Mater. Struct. 38 (1) (2005) 47–56.
[48] A. Meda, F. Minelli, G. Plizzari, P. Riva, Shear behaviour of steel fibre reinforced concrete beams, Mater. Struct. 38 (3) (2005) 343–351.
[49] T.D. Dang, D.T. Tran, L. Nguyen-Minh, A.Y. Nassif, Shear resistant capacity of steel fibres reinforced concrete deep beams: An experimental investigation and a new prediction model, in: Structures, Vol. 33, Elsevier, 2021, pp. 2284–2300.
[50] J.A. Torres, E.O. Lantsoght, Influence of fiber content on shear capacity of steel fiber-reinforced concrete beams, Fibers 7 (12) (2019) 102.
[51] F. Minelli, A. Conforti, E. Cuenca, G. Plizzari, Are steel fibres able to mitigate or eliminate size effect in shear? Mater. Struct. 47 (3) (2014) 459–473.
[52] D.-K. Thai, D.-L. Nguyen, D.-D. Nguyen, A calibration of the material model for FRC, Constr. Build. Mater. 254 (2020) 119293.
[53] L.J. Malvar, J.E. Crawford, J.W. Wesevich, D. Simons, A plasticity concrete material model for DYNA3D, Int. J. Impact Eng. 19 (9–10) (1997) 847–873.
[54] X. Lin, R.J. Gravina, An effective numerical model for reinforced concrete beams strengthened with high performance fibre reinforced cementitious composites, Mater. Struct. 50 (5) (2017) 1–13.

[55] L. Yang, X. Lin, R.J. Gravina, Evaluation of dynamic increase factor models for steel fibre reinforced concrete, Constr. Build. Mater. 190 (2018) 632–644.
[56] M. Petracca, F. Candeloro, G. Camata, STKO User Manual, ASDEA Software Technology, Pescara, Italy, 2017.
[57] M. Petracca, L. Pelà, R. Rossi, S. Zaghi, G. Camata, E. Spacone, Micro-scale continuous and discrete numerical models for nonlinear analysis of masonry shear walls, Constr. Build. Mater. 149 (2017) 296–314.
[58] J. Oliver, A consistent characteristic length for smeared cracking models, Internat. J. Numer. Methods Engrg. 28 (2) (1989) 461–474.
[59] Z.P. Bažant, B.H. Oh, Crack band theory for fracture of concrete, Matér. Constr. 16 (3) (1983) 155–177.
[60] C. Lassi, Studio Con il Metodo degli Elementi Finiti dell'Accoppiamento Forzato Ruota Sala Ferroviaria (Master Thesis, AA 1994-1995), Dipartimento Di Meccanica, Politecnico Di Milano, 1995.
[61] K.-J. Bathe, Finite Element Procedures, Vol. 1037, Prentice-Hall, New Jersey, 1996, p. 1.
[62] H. Nguyen, M. Pathirage, M. Rezaei, M. Issa, G. Cusatis, Z.P. Bažant, New perspective of fracture mechanics inspired by gap test with crack-parallel compression, Proc. Natl. Acad. Sci. 117 (25) (2020) 14015–14020.
[63] L. Sorelli, A. Meda, G. Plizzari, Bending and uniaxial tensile tests on concrete reinforced with hybrid steel fibers, J. Mater. Civ. Eng. 17 (5) (2005) 519–527.
[64] A. Carpinteri, F. Accornero, Rotation versus curvature fractal scaling in bending failure, Phys. Mesomech. 22 (2019) 46–51.
[65] J. Barros, J. Figueiras, Dramix steel fibre reinforced industrial floor design in accordance with the concrete society TR34, 1997.
[66] A. Carpinteri, F. Accornero, Dimensional analysis of critical phenomena: Self-weight failure, turbulence, resonance, fracture, Phys. Mesomech. 24 (4) (2021) 459–463.
[67] F. Accornero, A. Rubino, A. Carpinteri, Ductile-to-brittle transition in fibre-reinforced concrete beams: Scale and fibre volume fraction effects, Mater. Des. Process. Commun. 2 (6) (2020) e127.
[68] A. Carpinteri, Scaling laws and renormalization groups for strength and toughness of disordered materials, Int. J. Solids Struct. 31 (3) (1994) 291–302.
[69] Z.P. Bazant, J.-K. Kim, Size Effect in Shear Failure of Longitudinally Reinforced Beams, American Concrete Institute, 1984.
[70] A. Carpinteri, F. Accornero, The bridged crack model with multiple fibres: Local instabilities, scale effects, plastic shake-down, and hysteresis, Theor. Appl. Fract. Mech. 104 (2019) 102351.
[71] A. Carpinteri, Stability of fracturing process in RC beams, J. Struct. Eng. 110 (3) (1984) 544–558.
[72] F. Accornero, R. Cafarelli, A. Carpinteri, The cohesive/overlapping crack model for plain and reinforced concrete beams: Scale effects on cracking and crushing failures, Mag. Concr. Res. 74 (9) (2022) 433–450.
[73] A. Carpinteri, F. Accornero, R. Cafarelli, Scale-dependent maximum reinforcement percentage in RC beams, Struct. Concr. 22 (2021) 2155–2166.
[74] Eurocode 2: Design of concrete structures - part 1-1: General rules - rules for buildings, bridges and civil engineering structures, 2021.